INSTITUTE OF PHYSICS PUBLISHING CLASSICAL AND QUANTUM GRAVITY

Class. Quantum Grav. **23** (2006) 3333–3352 doi:10.1088/0264-9381/23/10/006

Critical collapse of an ultrarelativistic fluid in the $\Gamma \to 1$ limit

Martin Snajdr

Department of Physics and Astronomy, University of British Columbia, Vancouver, BC, V6T 1Z1, Canada

Received 16 August 2005, in final form 20 March 2006
Published 19 April 2006
Online at stacks.iop.org/CQG/23/3333

Abstract

In this paper, we investigate the critical collapse of an ultrarelativistic perfect fluid with the equation of state $P = (\Gamma - 1)\rho$ in the limit of $\Gamma \to 1$. We calculate the limiting continuously self-similar (CSS) solution and the limiting scaling exponent by exploiting self-similarity of the solution. We also solve the complete set of equations governing the gravitational collapse numerically for $(\Gamma - 1) = 10^{-2}, \ldots, 10^{-6}$ and compare them with the CSS solutions. We also investigate the supercritical regime and discuss the hypothesis of naked singularity formation in a generic gravitational collapse. The numerical calculations make use of advanced methods such as high-resolution shock capturing evolution scheme for the matter evolution, adaptive mesh refinement and quadruple precision arithmetic. The treatment of vacuum is also nonstandard. We were able to tune the critical parameter up to 30 significant digits and to calculate the scaling exponents accurately. The numerical results agree very well with those calculated using the CSS ansatz. The analysis of the collapse in the supercritical regime supports the hypothesis of the existence of naked singularities formed during a generic gravitational collapse.

PACS numbers: 04.20.Dw, 04.25.Dm, 04.40.Nr, 04.70.Bw, 02.60.−x, 02.60.Cb

1. Introduction

Since the discovery of critical phenomena in gravitational collapse of a massless scalar field by Choptuik in 1993 [1], researchers have observed critical phenomena in many different matter models. In this paper we focus on perfect fluid, in particular the ultrarelativistic perfect fluid with the equation of state

$$P = (\Gamma - 1)\rho. \tag{1.1}$$

The study of critical phenomena in ultrarelativistic perfect fluids has quite an interesting history. It started with Evans and Coleman's calculations [2] who were able to obtain a critical solution for the radiation fluid ($\Gamma = 4/3$) by employing the continuously self-similar (CSS) ansatz and also by directly solving the PDEs. Later, Koike *et al* [3] used perturbation analysis to calculate the scaling exponent of the radiation fluid collapse. Maison [4] generalized the calculations for $1.01 < \Gamma < 1.888$ and a similar analysis was carried out by Hara, Koike and Adachi [5]. Both speculated that the solutions might not exist for $\Gamma > 1.89$. A fully numerical treatment of the collapse for $1.05 < \Gamma < 1.5$ was performed by Evans and Perkins [6]. The inability to obtain solutions for $\Gamma > 1.89$ led to various ideas about what happens in that regime. Some proposed that the solution changes from CSS to DSS (discretely self-similar) or a mixture of both. It was also proposed that the critical solution might be of type I and not type II.

The confusion was definitely resolved by Neilsen and Choptuik [7] who demonstrated by directly solving the PDEs that nothing special happens for $\Gamma > 1.89$. They carried out the calculations all the way up to $\Gamma = 2$. Moreover, they were able to obtain the solutions for $\Gamma > 1.89$ with the CSS ansatz. The key to success was to use arbitrary precision arithmetic.

The purposes of this paper are several. We confirm the results of the perturbation calculations with the CSS ansatz from previous works for values of Γ close to 1 and, more importantly, we confirm by direct numerical collapse calculations that the perturbative calculations give the correct solutions for that regime. We obtain the exact numerical value of the limiting scaling exponent that has never been calculated before.

One of the reasons for studying the $\Gamma \to 1$ limit is to verify the hypothesis made by Harada and Maeda that for $\Gamma < 1.0105$ the final state of a supercritical collapse is not a black hole but a naked singularity [8, 9]. It is known that the critical solution contains a naked singularity but this is only achieved by fine tuning of the critical parameter. The naked singularity formed during the supercritical collapse would not require any fine tuning and therefore is much more interesting.

Critical collapse possesses a unique set of challenges for numerical treatment. During the evolution, the dynamics occurs on ever-decreasing length scales and the magnitudes of the fluid state variables increase by many orders. Therefore, advanced numerical techniques have to be used to perform these calculations.

For this purpose, we develop a general adaptive mesh refinement (AMR) algorithm which is capable of performing the critical collapse calculations. This algorithm is general and does not rely on prior knowledge of the dynamics. We also use an innovative treatment of vacuum that does not use a low-density artificial atmosphere—a method widely used to ameliorate numerical instabilities at the matter–vacuum boundary.

The use of quadruple precision arithmetic and the above-described advanced numerical techniques allows us to obtain the solutions and scaling exponents with higher accuracy than in previous works.

The organization of the paper is as follows. Section 2 reviews the basic equations of general relativistic hydrodynamics in spherical symmetry. In section 3, we sketch the ideas behind the CSS ansatz and present the equations and their solutions for the limiting case $\Gamma \to 1$. Similarly, in section 4 we briefly review the perturbation theory and present the equations and their solutions for the relevant eigenmodes in the limiting case. In the later two sections, we closely follow the approach described in [5, 10] where all of the missing details can be found. Section 5 describes the method of obtaining the critical scaling exponent from numerical calculations and a way of estimating the errors. It summarizes and compares results obtained from both approaches. We also compare our numerical results from supercritical calculations with the expected CSS solutions. Section 6 summarizes the results and concludes.

The appendix describes in more detail some of the features of the numerical algorithms such as AMR and vacuum treatment.

Throughout this paper we use geometrized units with $G = c = 1$.

2. Hydrodynamics in spherical symmetry

In our calculations we use spherical polar coordinates in which the metric has the form

$$ds^2 = -\alpha(t,r)^2\,dt^2 + a(t,r)^2\,dr^2 + r^2\,d\Omega^2. \tag{2.1}$$

It is convenient to define an auxiliary variable $m(t,r)$

$$m(t,r) = \frac{r}{2}\left(1 - \frac{1}{a(t,r)^2}\right), \tag{2.2}$$

which could be interpreted as the total mass enclosed within the radius r. In the vacuum regions we demand that the metric reduces to the Schwarzschild one, i.e.,

$$a(t,r) = -\frac{1}{\alpha(t,r)}. \tag{2.3}$$

The stress–energy tensor for perfect fluid has the form

$$T^{\mu\nu} = (\rho + P)u^\mu u^\nu + Pg^{\mu\nu}, \tag{2.4}$$

where P is the isotropic pressure, u^μ is the 4-velocity of the fluid element and ρ is the *total energy density* as seen by Eulerian observers (see later). The energy density ρ can be subdivided into two contributions

$$\rho = \rho_0(1 + \epsilon), \tag{2.5}$$

with ρ_0 being the *rest mass density* and ϵ being the *specific internal energy*. In the ultrarelativistic limit the internal energy contribution dominates the total energy density, i.e.,

$$\epsilon \gg 1. \tag{2.6}$$

The Eulerian observers' 4-velocity $u^\mu = n^\mu$, where n^μ is the unit normal vector to the spatial hypersurfaces defined by the constant time t slices. These observers see the fluid moving with the 3-velocity

$$v^r = \frac{u^r}{\alpha u^t}. \tag{2.7}$$

It is useful to define a velocity v as

$$v = av^r, \tag{2.8}$$

since the Lorentz factor is then a simple function of v:

$$W = \alpha u^t = \frac{1}{\sqrt{1 - v^2}}. \tag{2.9}$$

The equations of motion for the fluid can be derived from conservation laws

$$T^{\mu\nu}_{\ ;\nu} = 0, \tag{2.10}$$

$$J^\mu_{\ ;\mu} = 0, \tag{2.11}$$

where

$$J^\mu = \rho_0 u^\mu. \tag{2.12}$$

These equations must be supplemented with an equation of state which for perfect fluid has the form

$$P = (\Gamma - 1)\rho_0\epsilon. \tag{2.13}$$

In the ultrarelativistic limit described by (2.6) the equation of state has the form

$$P = (\Gamma - 1)\rho. \tag{2.14}$$

The equation of state (2.14) is the one we use. The set of *primitive variables* (ρ, v) characterizes the state of the fluid completely. Note that since ρ_0 does not enter the equation of state (2.14) equation (2.11) (baryon number conservation) is no longer needed for the dynamical evolution of ultrarelativistic fluid.

We define a complementary set of *conservative* fluid variables (S, E)

$$S = (\rho + P)W^2 v, \tag{2.15}$$

$$E = (\rho + P)W^2 - P. \tag{2.16}$$

The equations of motion for the fluid have the form

$$\dot{S} + \frac{1}{r^2}[r^2 X(Sv + P)]' = \Psi, \tag{2.17}$$

$$\dot{E} + \frac{1}{r^2}[r^2 XS]' = 0, \tag{2.18}$$

where

$$X = \frac{\alpha}{a} \tag{2.19}$$

and the source term Ψ has the form

$$\Psi = (Sv - E)\left(8\pi\alpha a r P + \alpha a \frac{m}{r^2}\right) + \alpha a P \frac{m}{r^2} + \frac{2\alpha P}{ar}. \tag{2.20}$$

The dot denotes differentiation with respect to the coordinate time whereas the prime denotes differentiation with respect to the radial coordinate r.

As has been argued in [7], in numerical applications it is convenient to work with derived conservative quantities

$$\Phi = E - S, \tag{2.21}$$

$$\Pi = E + S. \tag{2.22}$$

The equations of motion for these new variables have the form

$$\dot{\mathbf{q}} + \frac{1}{r^2}[r^2 X\mathbf{f}]' = \Sigma, \tag{2.23}$$

with

$$\mathbf{q} = \begin{pmatrix} \Pi \\ \Phi \end{pmatrix}, \qquad \mathbf{f} = \begin{pmatrix} \frac{1}{2}(\Pi - \Phi)(1 + v) + P \\ \frac{1}{2}(\Pi - \Phi)(1 - v) - P \end{pmatrix}, \qquad \Sigma = \begin{pmatrix} \Psi \\ -\Psi \end{pmatrix}. \tag{2.24}$$

The equations for the geometry can be obtained from the non-trivial component of the momentum constraint

$$\dot{a} = -4\pi r\alpha a^2 S, \tag{2.25}$$

the polar slicing condition

$$\frac{\alpha'}{\alpha} = a^2\left(4\pi r(Sv + P) + \frac{m}{r^2}\right) \tag{2.26}$$

and the Hamiltonian constraint

$$\frac{a'}{a} = a^2\left(4\pi r E - \frac{m}{r^2}\right). \tag{2.27}$$

In the numerical calculations we use only equations (2.26) and (2.27), i.e., we use a fully constrained evolution for the geometry.

3. CSS solutions

Under the assumption that the critical solutions are continuously self-similar we can transform the system of PDEs (2.23) and (2.25)–(2.27) into a system of ODEs that can then be solved numerically. Once the critical solution is found it is possible to solve for linear perturbation modes. The *relevant mode* is the mode that has the eigenvalue with the largest real part. There exists a simple relation between the eigenvalue of the relevant mode and the scaling exponent

$$\gamma = \frac{1}{\kappa}, \tag{3.1}$$

where κ is the eigenvalue of the relevant mode (in our case it is a real number).

Let us now briefly summarize the procedure for finding the CSS solutions. The details can be found in [5]. We can rewrite equations (2.23), (2.25)–(2.27) in terms of new variables adapted to the CSS symmetry

$$s = -\ln(-t_*), \tag{3.2}$$

$$x = \ln\left(-\frac{r}{t_*}\right). \tag{3.3}$$

The time coordinate t_* is fixed by the requirement that the collapsing CSS solution reaches the origin at time $t_* = 0$ and that the sonic point is always located at $x = 0$. Using a new set of variables

$$N = \frac{\alpha}{a\,\mathrm{e}^x}, \tag{3.4}$$

$$A = a^2, \tag{3.5}$$

$$\omega = 4\pi r^2 a^2 \rho, \tag{3.6}$$

we can write the system

$$\frac{A_{,x}}{A} = 1 - A + \frac{2\omega(1 + (\Gamma - 1)v^2)}{1 - v^2}, \tag{3.7}$$

$$\frac{N_{,x}}{N} = -2 + A - (2 - \Gamma)\omega, \tag{3.8}$$

$$\frac{A_{,s}}{A} + \frac{A_{,x}}{A} = -\frac{2\Gamma N v\omega}{1 - v^2}, \tag{3.9}$$

$$\frac{(\Gamma - 1)v}{\omega}\omega_{,s} + \frac{(1 + Nv)}{\omega}\omega_{,x} + \frac{\Gamma(N + v)}{1 - v^2}v_{,x} = \frac{3(2 - \Gamma)}{2}Nv - \frac{2 + \Gamma}{2}ANv + (2 - \Gamma)Nv\omega, \tag{3.10}$$

$$\frac{(\Gamma-1)v}{\omega}\omega_{,s}+\frac{\Gamma}{1-v^2}v_{,s}+(\Gamma-1)\frac{N+v}{\omega}\omega_{,x}+\frac{\Gamma(1+Nv)}{1-v^2}v_{,x}$$
$$=(2-\Gamma)(\Gamma-1)N\omega\frac{7\Gamma-6}{2}N+\frac{2-3\Gamma}{2}AN. \tag{3.11}$$

These equations are not independent—equation (3.9) is automatically satisfied if the rest of them are providing the solutions satisfy the boundary conditions

$$A(s,-\infty)=1, \qquad v(s,-\infty)=\omega(s,-\infty)=0. \tag{3.12}$$

For a CSS solution, all of the variables (N, A, v, ω) are functions of x only therefore equations (3.7)–(3.11) reduce to a set of ODEs

$$\frac{A_{,x}}{A}=1-A+\frac{2\omega(1+(\Gamma-1)v^2)}{1-v^2}, \tag{3.13}$$

$$\frac{N_{,x}}{N}=-2+A-(2-\Gamma)\omega, \tag{3.14}$$

$$\frac{A_{,x}}{A}=-\frac{2\Gamma Nv\omega}{1-v^2}, \tag{3.15}$$

$$\frac{(1+Nv)}{\omega}\omega_{,x}+\frac{\Gamma(N+v)}{1-v^2}v_{,x}=\frac{3(2-\Gamma)}{2}Nv-\frac{2+\Gamma}{2}ANv+(2-\Gamma)Nv\omega, \tag{3.16}$$

$$(\Gamma-1)\frac{N+v}{\omega}\omega_{,x}+\frac{\Gamma(1+Nv)}{1-v^2}v_{,x}=(2-\Gamma)(\Gamma-1)N\omega\frac{7\Gamma-6}{2}N+\frac{2-3\Gamma}{2}AN. \tag{3.17}$$

From (3.13) and (3.15) an algebraic equation can be formed

$$(1-A)(1-v^2)+2\omega(1+(\Gamma-1)v^2)=-2\Gamma Nv\omega, \tag{3.18}$$

which can, in principle, be used to eliminate one of the variables. We will label the CSS solutions as $(N_{ss}, A_{ss}, v_{ss}, \omega_{ss})$.

We are interested in solutions with Γ close to 1. In what follows it is convenient to define a new parameter

$$k=\sqrt{\Gamma-1}. \tag{3.19}$$

Our strategy is to expand the CSS solutions in powers of k. We can deduce the leading terms by looking at solutions for k close to zero. Our ansatz is

$$N_{ss}=\frac{\bar{N}_0\,\mathrm{e}^{-x}}{k}, \tag{3.20}$$

$$A_{ss}(x)=1+\bar{A}(x)k^2, \tag{3.21}$$

$$w_{ss}(x)=\bar{\omega}(x)k^2, \tag{3.22}$$

$$v_{ss}(x)=\bar{v}(x)k. \tag{3.23}$$

Substituting expressions (3.19)–(3.23) into equations (3.13)–(3.18) and keeping only the leading terms we obtain the equations for $\bar{\omega}$ and $\bar{v}$:

$$(1+\bar{N}_0\,\mathrm{e}^{-x}\bar{v})\bar{\omega}_{,x}+\bar{N}_0\,\mathrm{e}^{-x}\bar{\omega}\bar{v}_{,x}=0, \tag{3.24}$$

$$\frac{\bar{N}_0}{\bar{\omega}}\bar{\omega}_{,x}+(\mathrm{e}^x+\bar{N}_0\bar{v})\bar{v}_{,x}=-\bar{N}_0(\bar{\omega}+\bar{N}_0\bar{\omega}\bar{v}\mathrm{e}^{-x}-2). \tag{3.25}$$

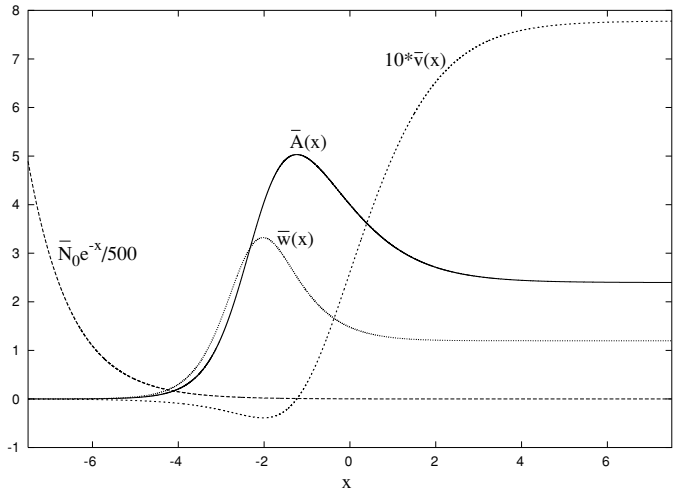

Figure 1. Plot of the limiting solutions of $\bar{N} = \bar{N}_0\,\mathrm{e}^{-x}$, $\bar{A}(x)$, $\bar{\omega}(x)$, $\bar{v}(x)$.

The algebraic equation (3.18) yields an expression for $\bar{A}$

$$\bar{A} = 2\bar{\omega}(1 + \bar{N}_0\,\mathrm{e}^{-x}\bar{v}), \tag{3.26}$$

which we used to eliminate $\bar{A}$ from the equations.

The scaling relations (3.20)–(3.23) are those of Newtonian CSS solutions. Indeed, equations (3.24)–(3.25) are exactly the CSS Newtonian equations as can be seen by comparison with equations (3.5)–(3.7) of [11] after the transformation $\bar{x} = -\mathrm{e}^{x}/\bar{N}_0$.

The numerical solutions of equations (3.24)–(3.25) are shown in figure 1. In this solution the velocity crosses the zero line once and it is the critical solution. It is the so-called Hunter's solution of type (a) [12].

4. Perturbations of the CSS solutions

Again, following [5] we calculate the relevant perturbations using a linear expansion

$$H(x, s) = H_{\mathrm{ss}}(x) + \epsilon h_{\mathrm{var}}(x, s), \tag{4.1}$$

where $H(x, s)$ is one of $\{\log(N), \log(A), \log(w), v\}$ and $h_{\mathrm{var}}(x, s)$ has the form

$$h_{\mathrm{var}}(x, s) = h_{\mathrm{p}}(x)\,\mathrm{e}^{\kappa s} \qquad \kappa \in \mathbb{C}. \tag{4.2}$$

The equations for $h_{\mathrm{p}}(x)$ are rather lengthy and can be found in [5] so we do not reproduce them here. Using the same strategy as in the previous section, we expand $h_{\mathrm{p}}(x)$ and κ in powers of k. The observed behaviour is

$$N_{\mathrm{p}}(x) = \bar{N}_{\mathrm{p}}(x), \tag{4.3}$$

$$A_{\mathrm{p}}(x) = \bar{A}_{\mathrm{p}}(x), \tag{4.4}$$

$$w_{\mathrm{p}}(x) = \frac{\bar{w}_{\mathrm{p}}(x)}{k^2}, \tag{4.5}$$

$$v_{\mathrm{p}}(x) = \frac{\bar{v}_{\mathrm{p}}(x)}{k}, \tag{4.6}$$

$$\kappa = \bar{\kappa} + O(k^2). \tag{4.7}$$

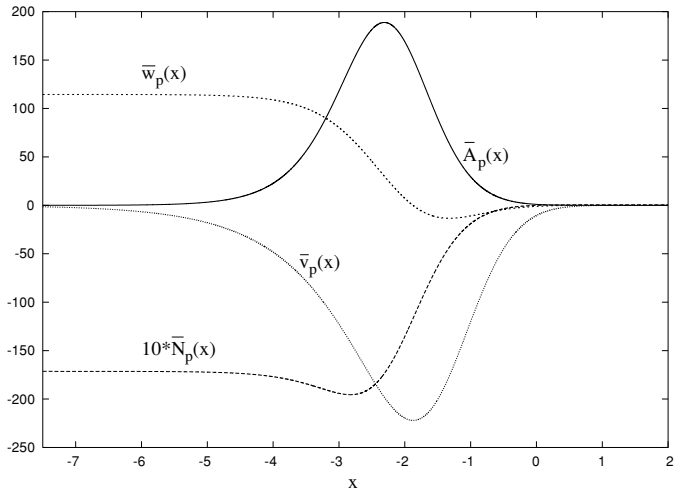

Figure 2. Plot of the relevant eigenmodes of the limiting CSS solution $\bar{N}_p(x)$, $\bar{A}_p(x)$, $\bar{\omega}_p(x)$, $\bar{v}_p(x)$.

After substituting (3.20)–(3.23) and (4.3)–(4.7) into the original equations and keeping only the leading terms we obtain a set of ODEs

$$\left[\begin{pmatrix} 1 & 0 & 0 & 0 \\ 0 & 1 & 0 & 0 \\ 0 & 0 & 1+\bar{N}_0\,\mathrm{e}^{-x}\bar{v} & \bar{N}_0\,\mathrm{e}^{-x} \\ 0 & 0 & \bar{N}_0\,\mathrm{e}^{-x} & 1+\bar{N}_0\,\mathrm{e}^{-x}\bar{v} \end{pmatrix}\frac{\mathrm{d}}{\mathrm{d}x} - \begin{pmatrix} -1 & 0 & 2\bar{\omega} & 0 \\ 1 & 0 & -\bar{\omega} & 0 \\ 0 & 0 & 0 & -\frac{\bar{N}_0\,\mathrm{e}^{-x}\bar{\omega}_{,x}}{\bar{\omega}} \\ -\frac{\bar{N}_0\,\mathrm{e}^{-x}}{2} & 0 & 0 & -\bar{N}_0\,\mathrm{e}^{-x}\bar{v}_{,x} \end{pmatrix}\right]\begin{pmatrix} \bar{A}_p \\ \bar{N}_p \\ \bar{w}_p \\ \bar{v}_p \end{pmatrix} = -\bar{\kappa}\begin{pmatrix} 0 & 0 & 0 & 0 \\ 0 & 0 & 0 & 0 \\ 0 & 0 & 1 & 0 \\ 0 & 0 & 0 & 1 \end{pmatrix}\begin{pmatrix} \bar{A}_p \\ \bar{N}_p \\ \bar{w}_p \\ \bar{v}_p \end{pmatrix}. \tag{4.8}$$

The algebraic equation has the form

$$(1-\bar{\kappa})\bar{A}_p - 2\bar{N}_0\,\mathrm{e}^{-x}\bar{\omega}(\bar{v}_p + \bar{v}\bar{\omega}_p) - 2\bar{\omega}\bar{\omega}_p = 0, \tag{4.9}$$

which can be used to verify the consistency of the results.

The solution methods for the limiting case are the same as described in [5]. In particular to solve for $\bar{v}(x)$ and $\bar{\omega}(x)$, we must regularize equations (3.24)–(3.25) at the sonic point ($x = 0$) and find the value of $\bar{v}(0)$ for which the solution has the correct behaviour as $x \to -\infty$. Similarly, the value of $\bar{\kappa}$ is found by requiring that $\bar{v}_p(x)$ does not diverge as $x \to -\infty$. To numerically integrate the set of ODEs we used the package LSODE [13, 14]. For increased precision we used 128 bit representation of floating point numbers (quadruple precision). Figure 2 shows the limiting solutions for the relevant eigenmodes.

5. Results of numerical calculations

Numerical modelling of type II critical collapse of relativistic fluids even in spherical symmetry is a rather challenging task. The reason is that the dynamics takes place at ever decreasing spatial length scale and also the density and pressure of the fluid increase by many orders of magnitude. For example, in our calculations the density and pressure increase typically by a

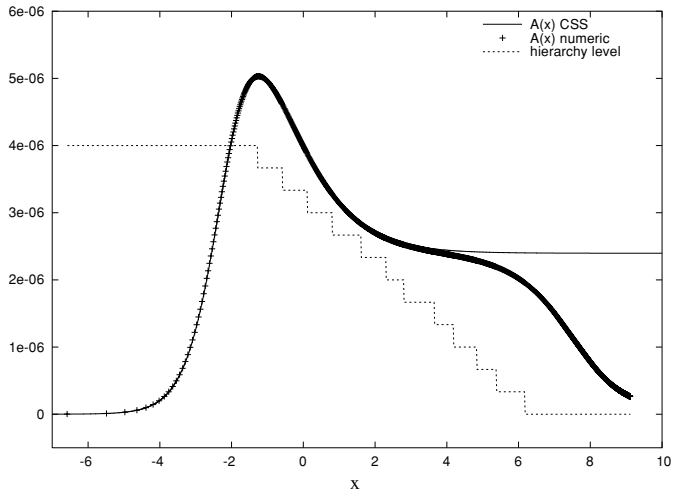

Figure 3. Comparison of CSS and numerical solution for $A(x)$ for $k^2 = 10^{-6}$.

factor of million for the nearly critical solutions (in the subcritical regime) and in some of the supercritical calculations the central density reached a value greater than 10^{54}. It is clear that some kind of adaptivity is required in order to perform these calculations.

For Γ close to 1, i.e., in the regime we want to explore, another difficulty arises—tuning the critical parameter to about 15 digits (the limit for double precision floating point numbers) is not sufficient and calculations in quadruple precision are necessary. This prolongs the runtime of the code significantly because on 'standard' workstations based on the x86 architecture quadruple precision is not natively supported by the processor. A more detailed description of some of the specifics of our numerical implementation can be found in the appendix.

5.1. Comparison of numerical and CSS critical solutions

If our numerical scheme works properly we should obtain the same critical solutions as we did by using the CSS ansatz (up to a truncation error). We must bear in mind, however, that the CSS critical solutions do not describe an asymptotically flat spacetime whereas the spacetime generated numerically is asymptotically Schwarzschild and therefore the solutions match only in a limited domain close to $r = 0$. In order to compare the solutions we have to translate the coordinate r used in numerical calculations into the self-similar coordinate x in which the CSS solutions are cast. The relation is provided by equation (3.3). Since the relation of t_* to t is not known we use some distinct features of the solution, e.g., local minimum or maximum to identify a particular r with a particular x. This allows us to calculate t_*.

Figures 3–6 show the comparison for $k^2 = 10^{-6}$. The numerical data were taken from the closest subcritical run just before the fluid dispersed. The numerical solutions agree very well with the CSS ones in a limited region as expected. The results for other values of k agree similarly well.

Note that the lapse α used in the numerical calculations is not the same as α from equation (3.4). Therefore in order to compare the functions $N(x)$ we must rescale one by a constant factor—we simply matched the leftmost data point from the numerical calculations with the corresponding one from the CSS solution. The dotted line shows the AMR hierarchy

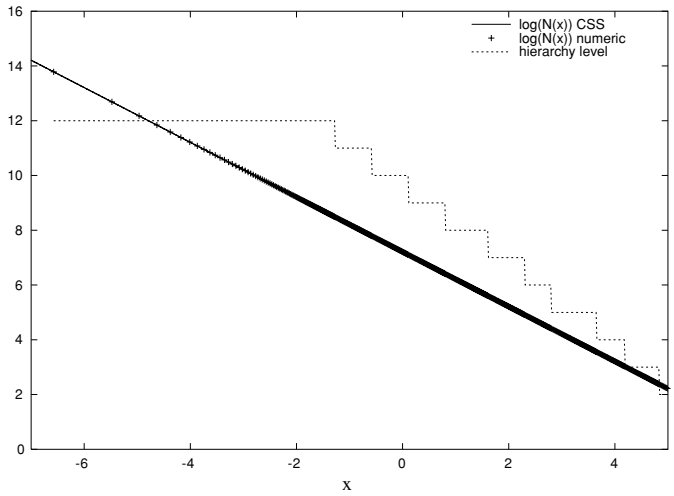

Figure 4. Comparison of CSS and numerical solution for $\log(N(x))$ for $k^2 = 10^{-6}$.

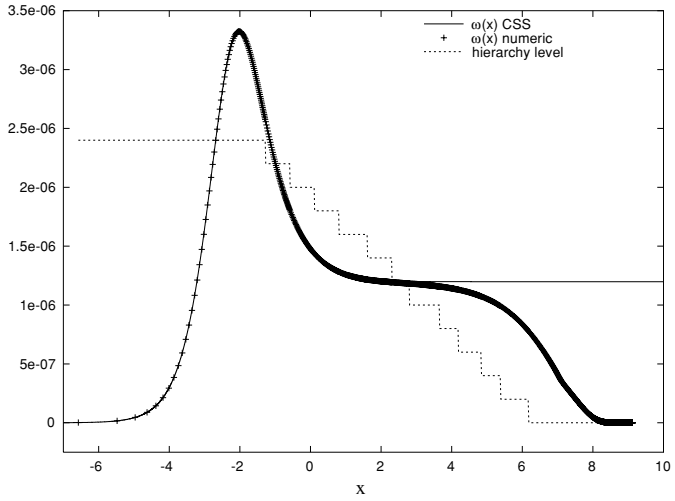

Figure 5. Comparison of CSS and numerical solution for $\omega(x)$ for $k^2 = 10^{-6}$.

level. An increase in the hierarchy level by 1 corresponds to a reduction of the cell size by a factor of 2.

5.2. Determining the scaling exponent

For the numerical calculations we chose the initial density profile to be a Gaussian:

$$\rho = p \exp[-(r - r_c)^2/\Delta^2], \tag{5.1}$$

and the velocity v was set to zero (we used $r_c = 0$ and $\Delta = 0.2$). The amplitude of the Gaussian p serves as the tunable parameter. Its critical value p_* can be found by a bisection search. Once the critical parameter is obtained with sufficient precision it is possible to calculate the scaling exponent.

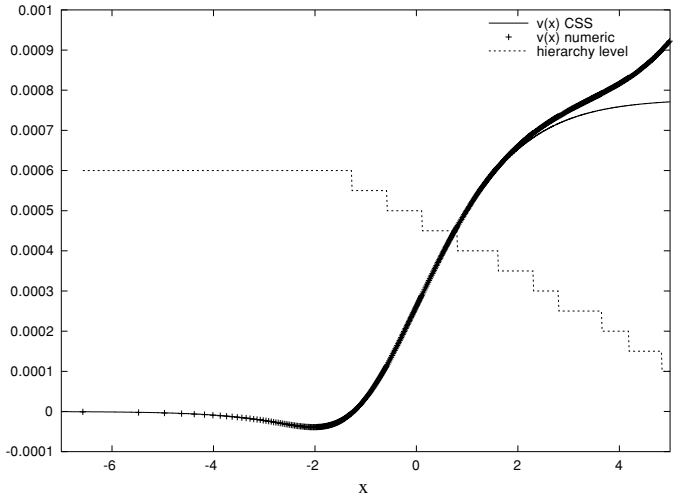

Figure 6. Comparison of CSS and numerical solution for $v(x)$ for $k^2 = 10^{-6}$.

We calculate the scaling exponent from *subcritical* runs. It has the obvious advantage that a black hole does not need to form in our spacetime (in our coordinate system it is not even possible). A further explanation will be given in the following section. The scaling relation for the trace of the stress–energy tensor has the form

$$\max\left(T^{\mu}{}_{\mu}\right) = 3P - \rho \sim |p - p_*|^{-2\gamma}. \tag{5.2}$$

An accurate determination of the scaling exponent in practice is not as straightforward as it might seem. The basic idea is to perform a number of subcritical runs and then fit a straight line to the logarithm of equation (5.2). In our approach we do not use a predetermined value of p_* but also optimize p_* in order to get the best fit. In that sense the fit is nonlinear.

We would like to have our data points separated approximately evenly in the $\log|p - p_*|$ coordinate but since we do not know the value of p_* beforehand we perform a trial fit to obtain the value of p_* and then use that value as a reference.

Another problem is to determine the interval of $\log|p - p_*|$ over which we perform the fit. A very broad interval is likely to give inaccurate results since the scaling behaviour is valid only in the vicinity of p_*. On the other hand fitting over a very narrow interval extremely close to p_* might produce incorrect results as well. We use the following approach which we believe is sufficiently robust and provides a way to estimate the error as well.

First we generate data points that span a rather wide range of $\log|p - p_*|$. Typically, we use around 100 data points. Then we perform what we call a *windowed fit*, i.e., fit data points with the index $i = k, \ldots, k + N_w - 1$ where $k = 1, \ldots, N - N_w + 1$. N_w is the width of the window and N is the total number of data points. If $N_w = N$ then the window spans all the data points.

Figure 7 shows data obtained from subcritical runs for $k^2 = 10^{-2}$. The dashed line (not very visible) corresponds to the best fit and yields a value of $\gamma_{\text{fit}} = 0.1148$. This is the value we report. Figure 8 shows γ as a function of k for various window sizes (different markers correspond to different window sizes). Each data point is plotted with an error bar corresponding to the error of each γ estimate that is equal to one-half of the standard deviation corresponding to the slope -2γ. The smaller the error bar the better the linear fit. The number of data points for each window size corresponds to the largest k of $N - N_w + 1$. The main

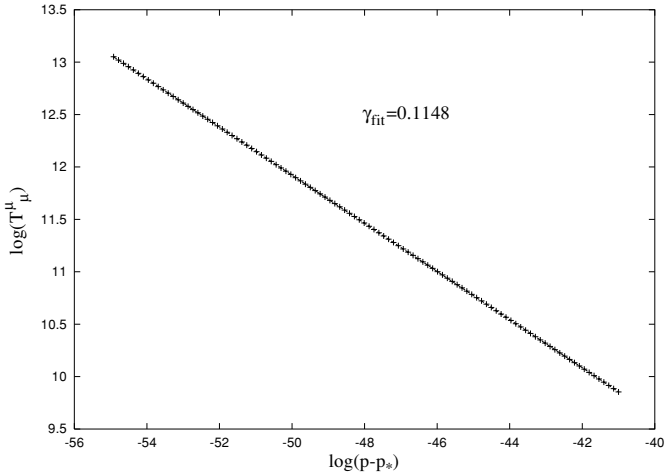

Figure 7. Fitted data from subcritical solutions for $k^2 = 10^{-2}$.

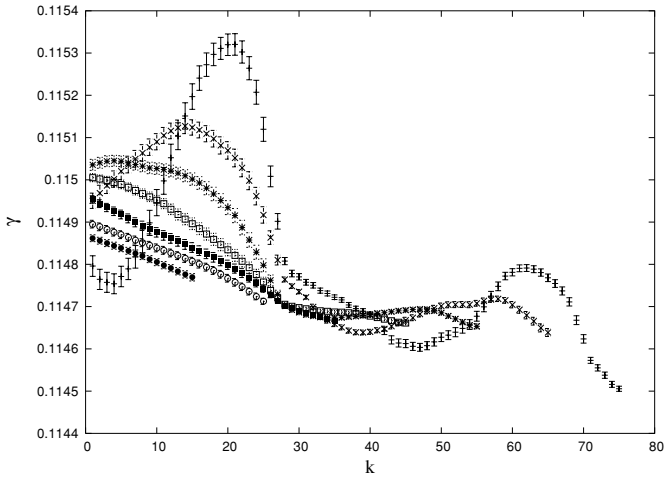

Figure 8. Windowed fits of data from subcritical runs for $k^2 = 10^{-2}$, $N_w = 30, 40, 50, 60, 70, 80, 90$.

purpose of this plot is to provide some quantitative estimate of the error of γ_{fit}. In addition, it may provide a hint whether there is some trend in γ as we fit data closer to the critical value p_*. Obviously, the largest variations are present for the smallest window sizes since we fit fewer data points. However, the averages

$$\gamma_{\text{av}} = \frac{1}{N - N_w + 1} \sum_{k=1}^{N-N_w+1} \gamma_k \tag{5.3}$$

for different window sizes N_w show very little variation. This is illustrated in figure 9.

Looking at figure 8 (although rather messy) we can very conservatively declare that for $k^2 = 10^{-2}$

$$\gamma < 0.1153. \tag{5.4}$$

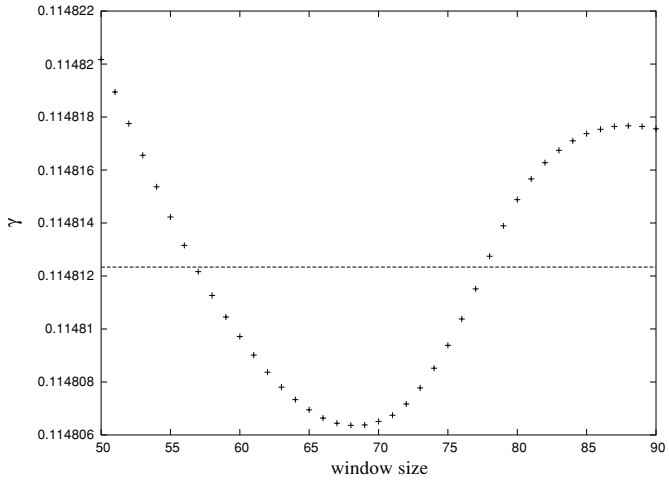

Figure 9. Averaged γ as a function of window size for $k^2 = 10^{-2}$.

Table 1. Scaling exponents calculated using both the CSS ansatz and a direct numerical solution. The values reported for $k = 0$ are the limiting values.

k^2	κ	γ_{ss}	γ_{fit}	Error (%)
10^{-2}	8.748 687 152	0.114 302 8643	0.1148	0.4
10^{-3}	9.386 603 219	0.106 534 8110	0.1071	0.5
10^{-4}	9.455 924 881	0.105 753 8012	0.1062	0.4
10^{-5}	9.462 917 038	0.105 675 6596	0.1062	0.5
10^{-6}	9.463 616 859	0.105 667 8451	0.1064	0.7
0	9.463 694 624	0.105 666 9768		

The plot also suggests a trend of decreasing γ as we fit data closer to p_*. Therefore it is not straightforward to estimate the lower bound for γ.

We created the same type of plots for all the other values of k. Their structure is similar; therefore we only show one additional set for $k^2 = 10^{-5}$ (figures 10–12). For $k^2 = 10^{-5}$ we do not see any obvious decreasing trend for γ. Moreover, we observe a drop in the γ value for the smallest window sizes plotted and large values of k. This just illustrates the fact that it could be dangerous to rely only on data from a narrow interval around the critical value p_*.

Table 1 summarizes the results obtained from both the perturbation theory (γ_{ss}) and the numerical calculations (γ_{fit}). The error reported is the percentage difference between γ_{ss} and γ_{fit}. Our results are in perfect agreement with [5] for the values of k reported therein.

5.3. The supercritical regime

In the previous section we showed how to calculate the critical exponents from subcritical runs using (5.2). Originally, the order parameter was taken to be the mass of a black hole formed during the supercritical collapse. Why have we not then used the supercritical runs and the black hole mass to determine the scaling exponent? Aside from the fact that in the coordinate system we are using we cannot really form a black hole, a more fundamental reason

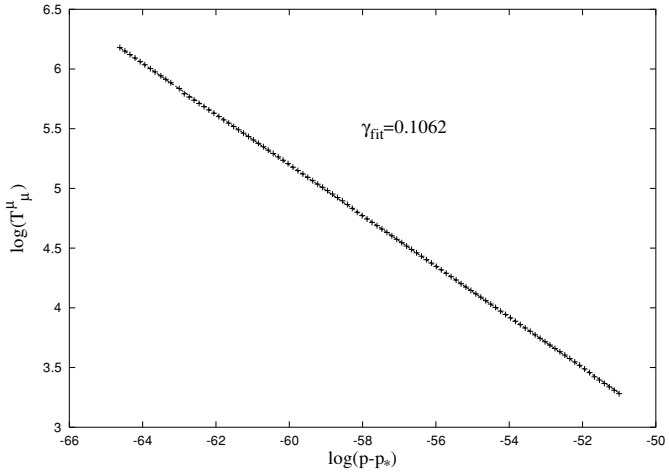

Figure 10. Fitted data from subcritical solutions for $k^2 = 10^{-5}$.

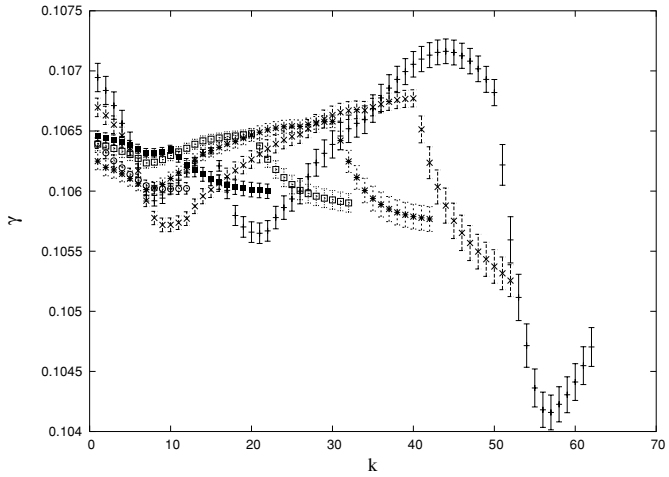

Figure 11. Windowed fits of data from subcritical runs for $k^2 = 10^{-5}$, $N_w = 40, 50, 60, 70, 80, 90$.

exists. There is no sign of black hole formation in the supercritical runs. Even after the central densities reach large values, there is no sign of event horizon formation (i.e. $2m/r$ approaches a constant value smaller than 1). According to [9] this is expected and the universal attractor is not a spacetime with a black hole but a general relativistic Larson–Penston (GRLP) solution. The GRLP solution exists only for $\Gamma - 1 < 0.036 \pm 0.002$ and it contains a naked singularity for $\Gamma - 1 < 0.0105$ [11].

The GRLP is a solution of equations (3.13)–(3.17) but unlike the critical solution (which is a general relativistic generalization of the Hunter's type (a) solution) it is a 'pure collapse' solution, i.e., the velocity is always negative.

To test this hypothesis, we performed a generic supercritical run for $\Gamma - 1 = 0.01$ and $\Gamma - 1 = 10^{-6}$. For $\Gamma - 1 = 10^{-6}$ we stopped the calculations when the refinement level reached 100. At that point the central density reached a value of about 10^{54} and the spatial

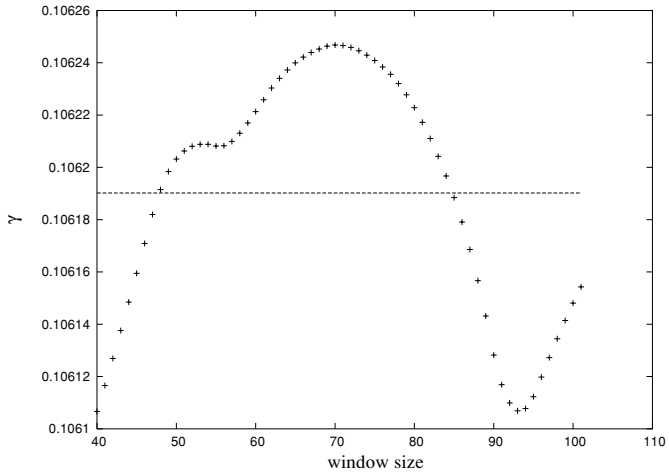

Figure 12. Averaged γ as a function of window size for $k^2 = 10^{-5}$.

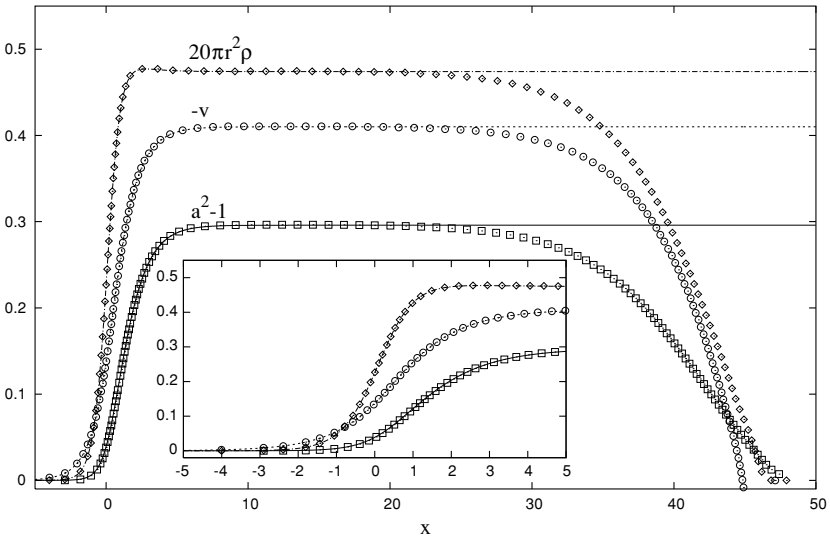

Figure 13. Comparison of the supercritical numerical solution and the GRLP solution for $\Gamma - 1 = 0.01$. The embedded plot shows details of the central region.

resolution at the centre was about 10^{-32}. For $\Gamma - 1 = 0.01$ we stopped the calculations at refinement level 65. The central density reached a value of about 10^{38} and the spatial resolution at the centre was about 10^{-22}. We stress that the calculations were stopped artificially and they could be, if needed, pushed further. We also performed a control supercritical run for $\Gamma - 1 = 0.02$ and we observed the quantity $2m/r$ approaching 1 as expected.

Figure 13 shows the comparison of the GRLP solution with the numerical data for $\Gamma - 1 = 0.01$. Figure 14 shows the comparison of the GRLP solution with the numerical data for $\Gamma - 1 = 10^{-6}$. In the plots we show only a fraction of the data points outside the very central region, so the GRLP solution is visible on the plots. The agreement is very good near the origin and starts to deviate at larger distances. This is expected since the GRLP solution is not asymptotically flat whereas the numerical solution is.

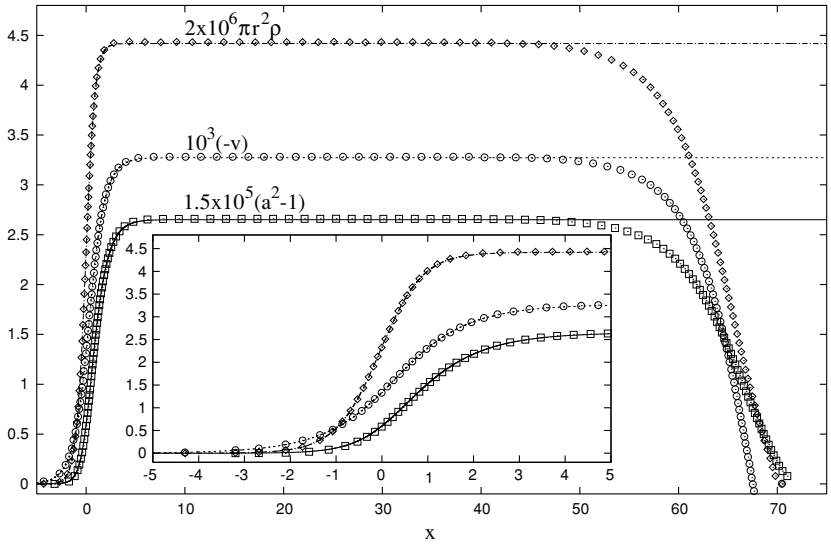

Figure 14. Comparison of the supercritical numerical solution and the GRLP solution for $\Gamma - 1 = 10^{-6}$. The embedded plot shows details of the central region.

These results support the hypothesis that the GRLP solution is an attractor for the supercritical collapse and therefore naked singularities can be formed in a generic gravitational collapse. It is conceivable that a black hole is also an attractor for the supercritical collapse. It would certainly be interesting to investigate the regime of the transition from GRLP to a black hole spacetime.

6. Conclusions

In this paper we calculated the critical solutions and scaling exponents for values of Γ close to 1 using both the CSS ansatz and by numerically solving the full set of equations for spherically symmetric ultrarelativistic fluid collapse. Moreover, by using the CSS ansatz we obtained and solved the equations for the limiting case $\Gamma = 1$. In the limit of $\Gamma \to 1$ the general relativistic critical solution converges to the Newtonian Hunters type (a) solution. The limiting value of the scaling exponent

$$\lim_{k\to 0} \gamma(k) = 0.105\,666\,9768 \tag{6.1}$$

can therefore be interpreted as the scaling exponent for critical collapse in Newtonian gravity. This is consistent with conclusions drawn from previous work [9, 11].

We also addressed the possibility of generic naked singularity formation in the supercritical regime. Our calculations support the fact that the supercritical collapsing solutions for $\Gamma - 1 \leqslant 0.01$ converge to the GRLP solution (and in the limit of $\Gamma \to 1$ to the Newtonian Larson–Penston solution) and from [11] then follows that these solutions contain a naked singularity. In other words, the GRLP solution is an endstate for a supercritical collapse of a slightly supercritical dataset for our family of initial data[1]. It would be interesting to further

[1] The values of the parameter p for the supercritical calculations were taken to be 0.1% larger than p_* for the $\Gamma - 1 = 10^{-6}$ runs and 4% larger than p_* for the $\Gamma - 1 = 10^{-2}$ runs. These values were chosen randomly and were not tuned in any way.

explore the structure of the solution space, in particular, to search for a supercritical collapse with a black hole as an endstate.

The numerically found solutions and scaling exponents agree very well (to a fraction of a per cent) with those obtained using the CSS ansatz. To numerically solve the equations we used advanced numerical methods including AMR, special vacuum treatment and quadruple precision floating point arithmetic.

Acknowledgments

This research was supported by the Natural Sciences and Engineering Research Council of Canada (NSERC) [20], the Canadian Institute for Advanced Research (CIAR) [21], the Alberta Science and Research Authority (ASRA) [22], the British Columbia Knowledge Development Fund (BCKDF) [23] and the University of British Columbia. In particular, some of the calculations described herein were run on CFI/ASRA/BCKDF funded hardware: the WestGrid cluster glacier.westgrid.ca [24] and the UBC PHAS/MECH cluster vnp4.physics.ubc.ca [25]. The author would like to thank Matt Choptuik, William Unruh and Carsten Gundlach for stimulating discussions and support of this work.

Appendix. Numerical scheme

Our numerical scheme for the fluid evolution is based on high-resolution shock capturing methods (HRSC) that have been used extensively in recent years. They are described in detail in numerous papers and review articles [15–18]. Therefore we are going to describe only those features of our code that are new or not completely obvious. All the calculations have been performed with quadruple precision arithmetic in order to tune the critical parameter p to as many as 30 significant digits.

We used AMR in order to follow the evolution on ever-decreasing spatial and time scales. Another feature we implemented was a 'true' vacuum, i.e., in the vacuum regions we do not keep a small residual fluid atmosphere (a so-called *floor*) but the fluid variables are set to zero values.

The regularity conditions for fluid variables are achieved by using *reflective* boundary conditions at the origin $r = 0$. We use *outflow* boundary conditions at the outer boundary (although there should be no fluid crossing the outer boundary).

To solve for the geometry we first solve for a using equation (2.27). We demand that $a(r = 0) = 1$ and integrate the equation outwards. α is obtained from equation (2.26) by integrating it inwards. It is initialized by setting $\alpha(r = r_{\max}) = -1/a(r = r_{\max})$.

A.1. Implementation of AMR

Our implementation of AMR can be viewed as an evolution on a dynamically changing non-uniform grid with a hierarchical structure[2]. We use a single global time step that is determined by the size of the smallest cell.

The grid structure changes if certain criteria are not met. The tests are performed at every fixed number of steps (at a *checkpoint*). The criteria we first implemented were based on the truncation error estimate. We compare a one-step update on a 2:1 coarsened grid with two-step update on the original grid. The problem with this approach was that occasionally

[2] In this context a hierarchical grid is a grid in which the size of two neighbouring cells may differ at most by the refinement ratio (in our case 2).

we experienced problems with the update during the coarse grid step. This certainly could be fixed but we opted for simpler criteria. In essence we want to guarantee that all the features of the solutions are well resolved. We demand higher resolution in regions with larger differences in gradients of the variables. The cells that do not meet our criteria are flagged (we can use more than one criterion).

After flagging we apply *buffering*, i.e., we flag nearby regions around the originally flagged cells. The size of the buffer regions is chosen so that each of the flagged cells could affect at most the cells within the buffer region during the evolution until the next checkpoint. Or, equivalently, we can say that only information from the buffer region could have reached the flagged cell during evolution from the previous checkpoint.

After the buffering step the grid is adjusted so that all the flagged cells are refined (we use 2:1 refinement ratio). We demand that the refinement algorithm preserves the hierarchical structure.

At this point we restart the evolution from the last *successful* checkpoint but with the newly created grid. All the variables are interpolated onto the new grid. If no cells were flagged (the grid is not changed) then the current state is stored (the grid structure and all the variables) and the evolution continues.

In systems where discontinuities may be present we must be a little bit more careful with the refinement scheme. Typically, our criteria would always fail at discontinuities and therefore a naive application of the aforementioned rules would lead to an uncontrolled refinement (in practice, we always set a maximum refinement level). This is not desirable since this would slow down the evolution tremendously. Moreover, our scheme is 'shock capturing' therefore it should treat discontinuous solutions properly. In general this issue is non-trivial and some clever scheme must be applied to deal with this. Our situation is slightly easier since we qualitatively know the dynamics. Although we do not expect shocks in the critical solutions we do have shocks in the computational domain. These are present in the 'outer domain', i.e., beyond the central self-similar region. We therefore employ a simple approach—we introduce different refinement maxima for the inner and outer regions (the outer region maximum is much smaller than the inner one).

A.2. Treatment of the vacuum

Vacuum regions always pose a problem in numerical hydrodynamics. Technically, the problem is that in very rarefied regions one part of the numerical scheme fails—in particular the conversion from conservative to primitive variables. It simply happens that there are no physical values of the primitive variables that correspond to the updated conservative variables. These regions are, however, dynamically completely unimportant since the energy and momentum densities there are negligible.

A standard approach is to maintain a minimal 'atmosphere' of fluid everywhere with the density several orders of magnitudes smaller than the typical densities in the system. Although we believe that there is nothing wrong with this approach and it would most certainly work in our situation we tried to develop a different approach.

One nice feature of a 'true' vacuum is that there are no fluxes through the outer boundary and therefore no artificial reflections.

Of course we cannot really solve the problem because of the non-existence of the exact Riemann solution at the vacuum boundary region. What we propose is a set of ideas which typically work in practice. They are not universal and one might need to adjust them slightly for different systems. Sometimes not all of them need to be used. In general, the situation is more complicated with stiffer fluids ($\Gamma \to 2$) but we were able to use the scheme even for

critical collapse of an ideal fluid with $\Gamma = 2$. We also used this approach in 2D modelling of axisymmetric fluid accretion onto black holes and some preliminary 3D runs of neutron stars. For the type of systems studied in this paper ($\Gamma \to 1$) the scheme works in its simplest form.

The basic ideas are as follows:

(i) Set the flux between two vacuum cells to zero.
(ii) The flux between vacuum and non-vacuum cell is calculated using Tadmor's scheme (as described in [19]).
(iii) After the update of the conservative variables set to vacuum all cells with fluid levels below a certain threshold.

The purpose of item (ii) is to use a simple and robust update scheme which relies only on the characteristic speeds and not on the full spectral decomposition typically needed in Roe type solvers.

Often, the approach described above is sufficient. This was the case for all the calculations we performed for the purpose of this paper. Since we used quadruple precision and our fluid is extremely soft we did not even need to apply the rule number (ii).

Sometimes we run into problems even after applying the above ideas. In this case we should always try to adjust the vacuum threshold up to the maximum level we can afford without losing a significant amount of fluid in the system.

If we use AMR and we run into trouble at some cell we can flag the cell and invoke an 'emergency' refinement and restart, especially if the cell is not at the vacuum boundary. We used this approach when we tested the numerical scheme on $\Gamma = 2$ ideal fluid. If the difficulty arises at the vacuum boundary (which happens in the majority of cases) we can simply set the cell to the vacuum values.

In general, it is likely that the velocities near the vacuum boundary will not be smooth and will be highly relativistic but this should not have any adverse effect on the dynamics (as long as the scheme works).

References

[1] Choptuik M W 1993 *Phys. Rev. Lett.* **70** 9
[2] Evans C R and Coleman J S 1994 *Phys. Rev. Lett.* **72** 1782
[3] Koike T, Hara T and Adachi S 1995 *Phys. Rev. Lett.* **74** 5170
[4] Maison D 1996 *Phys. Lett.* B **366** 82
[5] Hara T, Koike T and Adachi S 1996 *Preprint* gr-qc/9607010
[6] Perkins T J W 1996 *Thesis* (unpublished)
[7] Neilsen D W and Choptuik M W 2000 *Class. Quantum Grav.* **17** 761
[8] Harada T 1998 *Phys. Rev.* D **58** 104015
[9] Harada T and Maeda H 2001 *Phys. Rev.* D **63** 084022
[10] Koike T, Hara T and Adachi S 1999 *Phys. Rev.* D **59** 104008
[11] Ori A and Piran T 1990 *Phys. Rev.* D **42** 1068
[12] Hunter C 1977 *Astrophys. J.* **218** 834
[13] Hindmarsh A C 1983 *Scientific Computing* ed R S Stepleman *et al* (Amsterdam: North-Holland) p 55
[14] Petzold L R 1983 *J. Sci. Stat. Comput.* **4** 136
[15] LeVeque R J 1992 *Numerical Methods for Conservation Laws* (Basle: Birkhaüser)
[16] LeVeque R J 1998 *Computational Methods for Astrophysical Fluid Flow, 27th Saas-Fee Advanced Course Lecture Notes* (Berlin: Springer)
[17] Ibáñez J M, Martí J M, Miralles J A and Romero J V 1992 *Approaches to Numerical Relativity* (Cambridge: Cambridge University Press) p 223
[18] Romero J V, Ibáñez J M, Martí J M and Miralles J A 1996 *Astrophys. J.* **462** 839
[19] Lucas-Serrano A, Font J A, Ibáñez J M and Martí J M 2004 *Astron. Astrophys.* **428** 703
[20] http://www.nserc.ca
[21] http://www.ciar.ca

[22] http://www.asra.gov.ab.ca
[23] http://www.aved.gov.bc.ca/bckdf
[24] http://www.westgrid.ca/
[25] http://laplace.physics.ubc.ca/vnp4/
[26] http://www.ubc.ca
[27] http://www.innovation.ca